

APPLICATIONS OF PHOTOGRAMMETRY AND REMOTE SENSING TECHNOLOGIES IN CHANG'E-4 MISSION

K. Di^{1,*}, Z. Liu¹, W. Wan¹, S. Gou¹, T. Yu², J. Wang², L. Li², C. Liu², B. Liu¹, M. Peng¹, Y. Wang¹, Z. Yue¹, X. He², S. Liu²

¹ State Key Laboratory of Remote Sensing Science, Aerospace Information Research Institute, Chinese Academy of Sciences, Beijing, China - (dikc, liuzq, wanwh, gousheng, liubin, pengman, wangyx716, yuezy)@radi.ac.cn

² Beijing Aerospace Control Center, Beijing, China - yuty.bacc@foxmail.com (T.Yu), 15210106156@139.com (J.Wang), lichunmail@163.com (L.Li), ckliu2005@126.com (C.Liu), hxm_at1991@163.com (X.He), 568431578@qq.com (S.Liu)

Commission III, ICWG III/II

KEY WORDS: Lunar Exploration, Chang'e-4 mission, Yutu-2 Rover, Photogrammetry, Remote Sensing, Topographic Mapping, Rover Localization, Mineral Retrieval

ABSTRACT:

This paper presents a brief overview of photogrammetry and remote sensing technologies and applications in the Chang'e-4 mission. The developed technologies, such as image matching, block adjustment, 3D mapping, spectral analysis and mineral retrieval, have been applied in topographic mapping, rover localization, and rover path planning, and directly supported daily surface operations of the Yutu-2 rover. The technologies and products have also been supportive in various scientific investigations, such as topographic evolution of Von Kármán crater, multi-scale crater morphologies, mineral composition of lunar deep materials, regolith maturity and space weathering effects, etc.

1. INTRODUCTION

The Chang'e-4 (CE-4) mission is the fourth mission in China's Chang'e lunar exploration program and the second soft landing mission. The CE-4 probe, composed of a lander and a rover, was launched on 8 December 2018, achieved the first farside landing on 3 January 2019 in Von Kármán crater within the South Pole-Aitken (SPA) basin (Wu et al., 2019; Di et al., 2019a). As of 9 March 2022, the rover Yutu-2 (Jade Rabbit-2) had traversed 1087.1 m and acquired numerous in-situ high-resolution images and spectral data of the science targets, such as craters, regolith, rocks, etc.

Photogrammetry and remote sensing technologies have been developed by several teams and greatly supported mission operations of the rover, e.g., terrain perception, hazard detection, path planning, rover localization and navigation, etc. (Liu et al., 2020; Wang et al., 2020; Yu et al., 2020; Di et al., 2020). The technologies and derived products have also directly supported various scientific investigations of the landing site, e.g., topographic evolution, crater morphologies, mineral composition of lunar deep materials, impact melt breccia, space weathering etc. (Di et al., 2019b; Jia et al., 2021; Lin et al., 2020a; Gou et al., 2020a, 2020b, 2020c; Lin et al., 2021).

This paper presents a brief overview of the developed photogrammetry and remote sensing technologies and applications in CE-4 mission. It is important to note that the paper is not a complete summary of the numerous applications of photogrammetry and remote sensing technologies and products, rather it is an overview of the representative applications in mission operations and scientific studies, to demonstrate that photogrammetry and remote sensing can make critical contributions to extraterrestrial exploration.

2. CHANG'E-4 LANDING SITE AND DATA

The SPA basin is the largest (2500 km in diameter, ~13 km in depth) and oldest impact basin on the Moon and is thought to have exposed lunar mantle materials according to numerical simulations (Melosh et al., 2017). Von Kármán crater is in the northwest of the SPA basin and has a diameter of 186 km. The in-situ explorations by the Yutu-2 rover provide a unique opportunity to reveal information about lunar deep materials and the evolution history of the SPA basin.

Before CE-4 landing, existing orbital mapping products, including Chang'e-2 Digital Elevation Model (DEM) and Digital Orthophoto Map (DOM) (Li et al., 2015; Ren et al., 2019), Lunar Reconnaissance Orbiter Camera (LROC) Narrow Angle Camera (NAC) images (Robinson et al., 2010; Speyerer et al., 2016), Lunar Orbiter Laser Altimeter (LOLA) DEM (Smith et al., 2010), and SLDEM2015 (Barker et al. 2016), were used for characterization of the landing site by multiple teams (e.g., Di et al., 2019c; Wu et al., 2020). Fig. 1 shows the context maps of the CE-4 landing site.

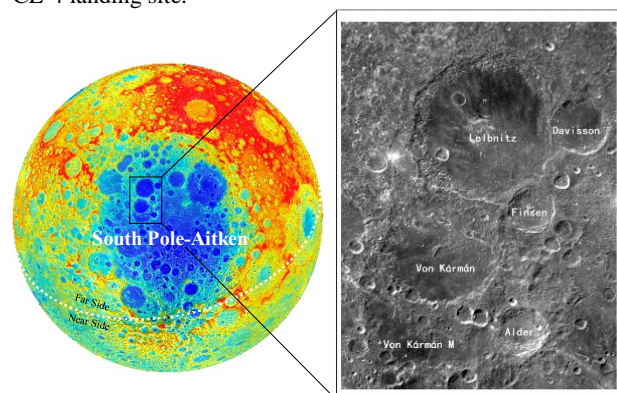


Figure 1. Context maps of CE-4 landing site. Left: LOLA DEM centered in the middle of the SPA basin, Right: Chang'e-2 DOM.

* Corresponding author

During the descent and landing process, the descent camera onboard the lander took 5300 images with resolutions from meter level to millimeter level. The downward-looking descent camera has a field of view (FOV) of 45.4° and an image size of 1024×1024 pixels. These images were used in lander localization and landing site mapping after landing.

The rover carries three pairs of stereo cameras, i.e., panoramic camera (Pancam), navigation camera (Navcam), and hazard avoidance camera (Hazcam). Pancam and Navcam are mounted on the camera bar atop the mast, both having a stereo base of 270 mm. Pancam has a FOV of 22.9° ×16.9° and an image size of 2352×1728 pixels (Jia et al. 2018). Navcam has the FOV of 46.6° and an image size 1024×1024 pixels. Hazcam is fixed on the lower front of the rover body with a baseline of 100mm; it has a FOV of 120° and an image size of 1024×1024 pixels (Yu et al., 2020).

Along the traverse, the rover obtains Navcam stereo images at every waypoint and acquires Pancam stereo images at some waypoints. These stereo images, with better than millimeter resolutions in near-range and centimeter resolutions in middle-range, have been routinely used in detailed topographic mapping and rover localization to support surface operations of the rover (Liu et al., 2020; Wang et al., 2020; Yu et al., 2020; Di et al., 2020).

The rover also carries a Visible and Near-Infrared Imaging Spectrometer (VNIS), consisting of a visible and near-infrared (VIS/NIR) imaging spectrometer and a shortwave infrared (SWIR) non-imaging spectrometer (Jia et al., 2018). The spectral range is 450–2395 nm with a sampling interval of 5 nm, and the total spectral channels is 400 (100 channels for the VIS/NIR and 300 channels SWIR) (He et al., 2019). In-situ VNIS data is acquired at designated science targets, e.g., regolith and rocks, to investigate their mineralogical compositions.

3. PHOTOGRAMMETRY TECHNOLOGIES AND APPLICATIONS

3.1 Topographic Mapping Using Orbital, Descent and Rover Images

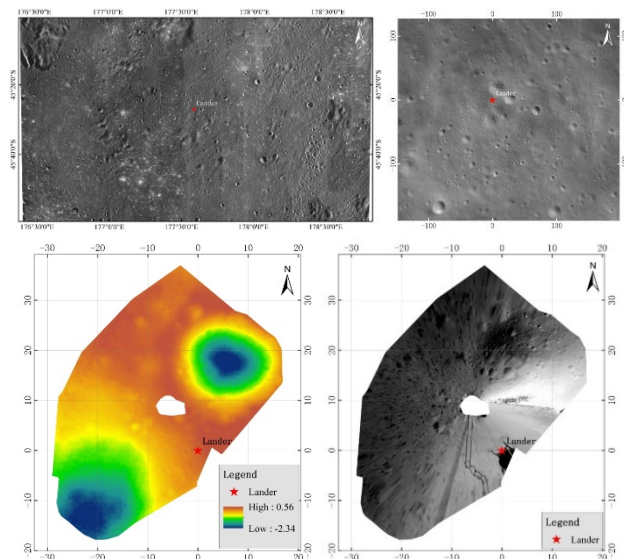


Figure 2. Topographic maps of CE-4 landing site of different scales (Liu et al., 2020). Upper left: LROC NAC DOM

(0.9m/pixel), Upper right: Descent DOM (0.1m/pixel), Lower left: Navcam DEM (0.02m/pixel), Lower right: Navcam DOM (0.02m/pixel).

Based on rigorous photogrammetric modelling and processing, a 0.9 m-resolution seamless DOM mosaic was produced using 100 LROC NAC images. A series of photogrammetric techniques, including rigorous sensor model construction, rational function model fitting, feature point matching and tie point selection, block adjustment, image ortho-rectification, and image mosaicking, were employed (Liu et al., 2018, 2019). The resultant seamless DOM has an images size of 57,483 columns × 34,084 rows and covers ~ 52 × 30 km (Fig.2 Upper left). This high-resolution DOM was used for detailed context analysis of the landing site, along with the existing orbital images and topographic products (Di et al., 2019c; Liu et al., 2020).

Complementary to the photogrammetric DEMs, Wu et al. (2020) generated a pixel-wise DEM of the CE-4 landing site using a 1.5 m/pixel LROC NAC image based on the shape-from-shading method with the 60m-resolution SLDEM as the constraint (Wu et al., 2018). This high-resolution DEM was used in geomorphologic analysis of the landing site, e.g., slope analysis and 3D measurements of small craters (Wu et al., 2020).

Photogrammetric bundle adjustment and ortho-rectification techniques were employed for descent images, and a DOM was generated from 100 descent images with a resampled resolution of 0.1 m and covering an area of 348 m × 315 m (Liu et al., 2020) (Fig.2 Upper right). This high resolution DOM was used in high precision localization of the lander and the rover and utilized as one of the basemaps for rover traverse planning.

Detailed topographic mapping was performed using rover images through photogrammetry techniques of feature extraction and matching, bundle block adjustment, dense matching, 3D point cloud generation, DEM interpolation, ortho-rectification, etc. (Liu et al., 2020). Local DEMs and DOMs with 0.02 m resolution were routinely generated using Navcam images at each waypoint in near real-time (e.g., Fig.2 Lower left and right). Subsequent detailed topographic analyses, including slope computation and hazard identification, were performed to support waypoint-to-waypoint path planning (Wang et al., 2020; Liu et al., 2020). High-resolution DEMs and DOMs were also produced using Pancam stereo images to support geomorphic analysis and science target selection (Di et al., 2019b).

3.2 Lander and rover localization

Immediately after landing, lander localization was conducted using orbital basemaps, descent images and monitoring camera image through image feature matching. The lander location was determined to be (177.588°E, 45.457°S) on the LROC NAC DOM (Di et al., 2019a). The CE-4 lander location was also determined on Chang'e-2 DOM and SLDEM2015. Later on, a LROC NAC image (M1303619844) was acquired on 1 February, 2019, in which the CE-4 lander can be directly observed. The lander localization result is almost the same as the actual location in the LROC NAC image, verifying the effectiveness and high precision of the lander localization method. The precise lander location was used as the origin to establish the landing site local coordinate system, based on which the rover-image-based mapping and localization have been performed.

The sequential descent images were also used for descent and landing trajectory recovery based on a self-calibration bundle adjustment method with the ground control points selected from

the LROC DOM and SLDEM2015 (Wan et al., 2019). The trajectory recovery results show that lander adjusted its attitude for the purpose of obstacle avoidance at the height of 2km and 100m. Comparison of the recovered trajectory data and telemetry data is valuable to evaluate the performance of descent and landing controls.

Localization of the rover with high accuracy is crucial to ensure safe traversing and effective approaching science targets. Three localization methods have been used to localize the rover on different turnaround times with different accuracies. The onboard dead-reckoning system uses wheel odometer and Inertial Measurement Unit (IMU) to derive the rover locations in real time. To reduce the localization error caused by wheel slippage and IMU drift, two visual positioning methods, namely cross-site visual localization and DOM matching, have been developed and routinely applied to localize the rover with high accuracy using the Navcam images (Wan et al., 2014; Liu et al., 2015, 2020).

The cross-site visual localization method is based on ASIFT feature matching and bundle adjustment of Navcam images acquired at adjacent sites (waypoints) (Wan et al. 2014). The DOM matching method is based on feature matching between a Navcam DOM and the orbital DOM basemap (Liu et al. 2015). The former has been applied in near real-time at each waypoint, while the latter was applied from time to time when landmarks (e.g., small craters and large rocks) are available in both Navcam and orbital DOMs. Figure 3 shows the traverse map of the rover as of 9 March 2022 (end of the rover's 40th lunar day). The traverse was based on the rover localization result from cross-site visual localization method and the DOM matching method.

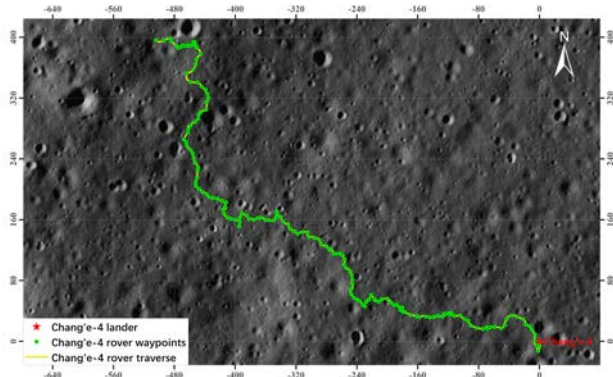


Figure 3. Traverse map of Yutu-2 rover as of 9 March 2022 (Unit: m).

3.3 Rover Path Planning

Detailed topographic mapping and analysis and rover localization directly contributed to rover path planning, ensuring safe and efficient traversing on the rugged lunar surface. During the mission operations, path planning was implemented by the teleoperation teams of Beijing Aerospace Control Center and China Academy of Space Technology. The rover path planning consists of overall planning, exploration period planning, and navigation unit planning (Yu et al. 2019). The high-accuracy rover locations and cm-resolution DEMs and derived slope maps have been the fundamental data for path planning through analysis of terrain traversability, hazard, illumination condition, communication attainability, etc.

3.4 Topographic Evolution of the Landing Site

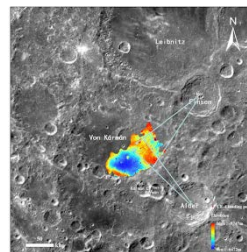


Figure 4. Topographic evolution of the landing site

A detailed topographic analysis of the landing site using a Pancam-image-derived 5 cm grid spacing DEM, existing orbital-data-derived DEMs, and numerical simulations revealed the topographic evolution of Von Kármán Crater. The interpretations and measurements show that the NE-SW ejecta from Finsen crater and the underlying SE-NW dome-like surface relief from Alder crater are superimposed on the base mare basalts within Von Kármán crater (Fig. 4). This superimposition relationship indicates that the surface material explored by the Yutu-2 rover should be lunar deep interior material excavated from the nearby Finsen crater with possible contributions from Alder crater, not the underlying mare basalt (Di et al., 2019).

3.5 Crater Statistics and Morphologic Investigation

Based on the multi-scale mapping products, a comprehensive morphologic investigation of impact craters in the CE-4 landing area was performed. As a result, 4333 craters larger than 100 m were mapped in the whole landing area (Fig.2 Upper left), 11787 several-meter scale craters were mapped in the local area (3.2 km × 3.0 km) surrounding the landing point (Fig. 5 Left), and 738 sub-meter to meter scale craters surrounding the rover were measured from the Pancam images taken at one waypoint (Jia et al., 2021).

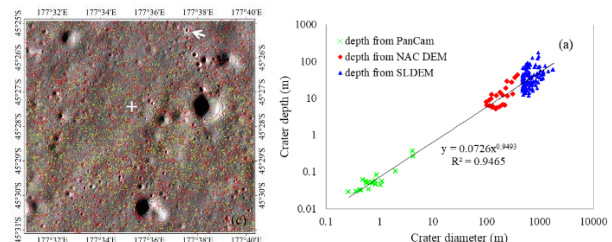


Figure 5. Left: The mapped craters in the 3.2 km×3.0 km area surrounding the CE-4 landing point. Right: The relationship between the diameter and the depth of craters. (Jia et al., 2021).

The crater size-frequency distribution reveals that craters smaller than 250 m of the whole landing area and smaller than 90 m within 3.2 km ×3.0 km area tend to reach saturation equilibrium. The relationship between the diameter and the depth of all depth-attainable craters is fitted with a power law (Fig. 5 Right); the resultant exponent is close to 1.0, indicating the depth and the diameter are almost linear. The comparison of d/D of the three sets of crater indicates that larger craters have relatively larger d/D, and small craters seem to be more easily to degrade or to be influenced by the target properties (Jia et al., 2021).

4. REMOTE SENSING TECHNOLOGIES AND APPLICATIONS

4.1 Mineral Retrieval Using In-Situ Spectral Data

The radiance spectra were processed by the solar irradiance calibration method to derive the full-range (450–2,395 nm) reflectance spectra of the science targets, e.g., regolith and rocks. Spectral analyses reveal that the regolith has a forsteritic olivine

(OL) and magnesium (Mg)-rich orthopyroxene (OPX) assemblage (Gou et al. 2020a) (Fig. 6).

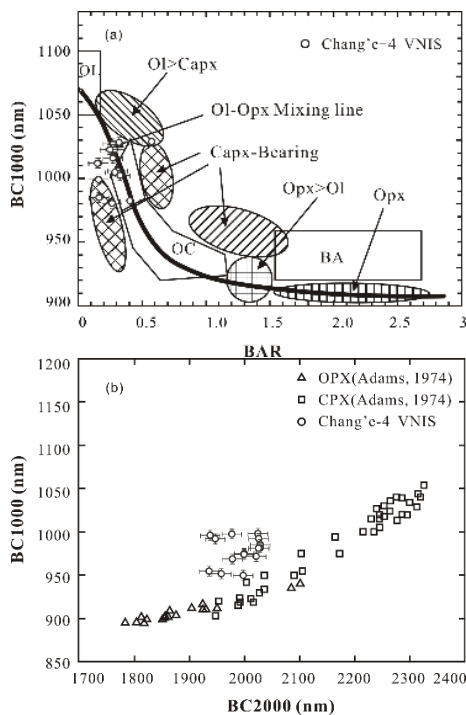


Figure 6. Scatter plots of spectral parameters: (a) BAR - BC1000; (b) BC2000 - BC1000. BAR: Band area ratio. BC1000: Absorption band center @ 1000 nm; BC2000: Absorption band center @ 2000 nm.

The SPA basin-forming event, which formed a transient crater of ~840 km in diameter and ~390 km in depth, should have sampled the lunar lower crust and upper mantle (Miljkovic et al., 2015). The impact-generated melt pool, which is chiefly the upper ~250 km of the lunar interior materials, likely differentiated and formed a noritic layer with a thickness of ~6 km and possibly as thick as ~13 km (Hurwitz and Kring, 2014). According to the surrounding topographic and geologic context (Fig. 4), the regolith at the landing site was primarily from the Finsen crater ejecta. Finsen crater is just about 370 km from the center of the SPA basin, meaning it is on the margin of the supposed transient crater. Therefore, the regolith at the landing site might originate from the lower base of a differentiated melt pool, or even from the lunar lower crust/upper mantle (Gou et al. 2020a).

4.2 Composition of the Unusual Substance

An unusual dark greenish and glistening substance was discovered in a fresh crater by the rover during the eighth lunar day (Fig. 7a). In appearance, the unusual substance, being 52 × 16 cm, especially resembles the lunar impact melt breccia samples returned by the Apollo missions. According to the impact simulation, the breccia may be formed by impact-generated welding, cementing and agglutinating of lunar regolith and breccia (Gou et al. 2020b). The impact melt breccia was confirmed by the presence of the glass-like spectrum by comparing with the spectra of the glass quenched from Apollo impact melt breccias (Fig. 7b) (Lin et al., 2020b). Yang et al. (2021) found the glassy material might have high concentration (47%) of carbonaceous chondrites, which was the remnants of the impactor.

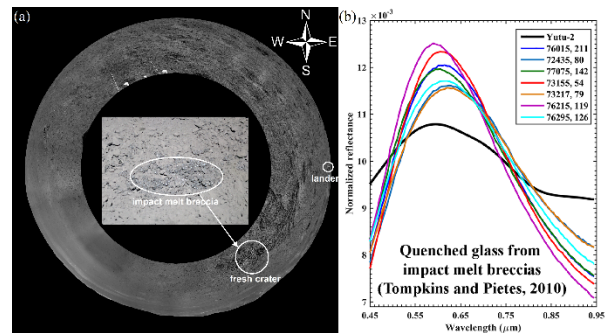


Figure 7. (a) Pancam mosaic of the unusual substance. (b) The comparison of the glassy fragments with glass quenched from Apollo impact melt breccias (Modified after Lin et al. 2020b).

4.3 Source of the Freshly Exposed but Geologically Old Rocks

The materials of the CE-4 landing area were chiefly from the 3.5 Ga Finsen crater ejecta, which should be turned into fine regolith within a few millions of years due to widespread small impacts and diurnal temperature cycling. However, Yutu-2 rover encountered light-toned rock fragments during its traverse inside the Von Kármán crater (Fig. 8a) and it made observations on two rock fragment samples at waypoints LE00303 and LE01310. Spectral signatures of the two measured rock fragments show a clear similarity in composition to the Imbrian Finsen crater materials (Fig. 8b). Some rock fragments encountered during the 13rd lunar day string out in long chains around a 15-m elliptical fresh crater, indicating they are ejecta of this secondary crater (Fig. 8c-d). It is proposed that these rock fragments are geologically old but freshly exposed (Gou et al., 2021). They might have a complex exposure history: born as Imbrian Finsen crater ejecta impact, possibly buried and resurfaced several times within Von Kármán by the churning mechanisms that continuously reshaped the lunar surface, and finally exhumed by a secondary impact from the Copernican 3.8-km Zhinyu crater.

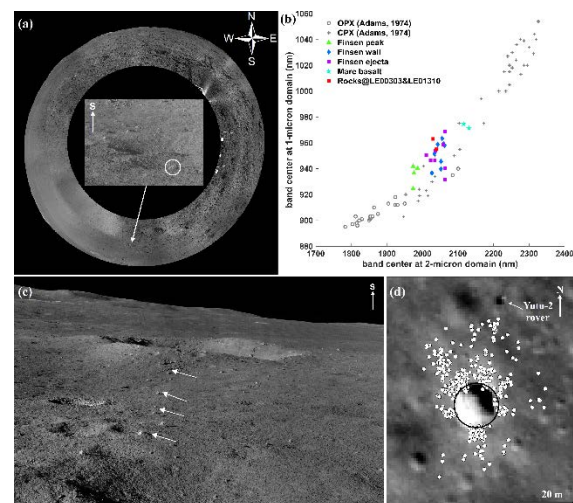


Figure 8. (a) Pancam mosaic generated from images acquired during the 13th lunar day. The rock fragment that was spectrally measured is indicated by the white circle. (b) Comparison of absorption band centers for different materials. (c) Pancam mosaics of the 15-m elliptical fresh crater with a blocky rim. (d) The spatial distribution of rock fragments around the 15-m crater. Each white dot represents a rock fragment. (Gou et al., 2021).

4.4 Regolith Maturity and Space Weathering Effects

In situ spectral measurements from Yutu-2 rover provide a unique opportunity to investigate the space weathering effects, which considerably darkens the reflectance, reddens the continuum slope and suppresses absorption features. Hapke model has been used to investigate the accumulated space weathering-induced submicroscopic metallic iron (SMFe) abundance in the regolith at the Chang'e-4 landing site. Simulation results reveal that the average SMFe abundance in the regolith is 0.32 ± 0.06 wt.% (Fig. 9a-b) (Gou et al., 2020c). The derived Is/FeO maturity index, which is 82 ± 15 , indicates the regolith at Chang'e-4 landing area is mature. By comparing LROC NAC images acquired both before and after the CE-4 probe landing, it is found that the lander rocket plume had modified the surface (Fig. 9c). However, the SMFe abundance in the regolith does not vary significantly with distance from the lander. The possible reason is that the fast gardening and impacting processes had sufficiently mixed the uppermost, finest, and highly mature particles in the landing area.

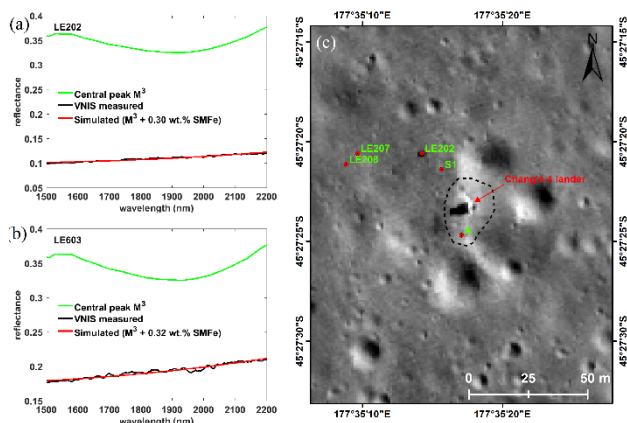


Figure 9. (a)-(b) Hapke model-derived space weathering-induced SMFe abundance at waypoints LE202 and LE603, respectively. (c) The region severely affected by rocket engine plume during soft landing (marked by the black dotted line). The basemap is LROC NAC image.

5. CONCLUSIONS

In CE-4 mission, photogrammetry and remote sensing technologies and products have made and will continue to make critical contributions to mission operations and scientific investigations. The meter level to cm level resolution topographic mapping product and the high-precision rover localization results are fundamentally important to support mission operations of the Yutu-2 rover for safe traversing on the rugged lunar surface, effective approaching science targets and in-situ scientific data acquisition. The spectral analysis based on VNIS data is essential to reveal the mineral compositions of the regolith and rocks, composition of the impact melt breccia, source of the freshly exposed but geologically old rocks, and space weathering effects at the landing site. The topographic and spectral analyses have been further contributed to understanding of the lunar deep materials and geologic evolution of Von Kármán crater.

ACKNOWLEDGEMENTS

The CE-4 mission was carried out by the Chinese Lunar Exploration Program, and the CE-4 data were supplied by the Science and Application Center for Moon and Deep Space Exploration, Chinese Academy of Sciences. The authors thank

the institutions/organizations for making the data used in this paper available. This work was supported in part by National Key Research and Development Program of China (Grant no. 2018YFB1305004), and National Natural Science Foundation of China (Grant no.s 41771488, 41771490 and 41941003).

REFERENCES

- Barker, M. K., Mazarico, E., Neumann, G. A., et al., 2016. A new lunar digital elevation model from the Lunar Orbiter Laser Altimeter and SELENE Terrain Camera. *Icarus*, 273, 346-355.
- Di, K., Liu, Z., Liu, B., et al. 2019a. Chang'e-4 lander localization based on multi-source data. *Journal of Remote Sensing*, 23(1): 177-184.
- Di, K., Zhu, M., Yue, Z., et al., 2019b. Topographic Evolution of Von Kármán Crater Revealed by the Lunar Rover Yutu - 2. *Geophysical Research Letters*, 46:12764-12770.
- Di, K., Liu Z., Liu B., et al, 2019c. Topographic analysis of Chang'e-4 landing site using orbital, descent and ground data. *Int. Arch. Photogramm. Remote Sens. Spatial Inf. Sci.*, XLII-2/W13, 1383-1387.
- Di, K., Liu, Z., Wan, W., et al., 2020. Geospatial technologies for Chang'e-3 and Chang'e-4 lunar rover missions. *Geo-spatial Information Science*, 23(1): 87–97.
- Gou, S., Di, K., Yue, Z., et al., 2020a. Forsteritic olivine and magnesium-rich orthopyroxene materials measured by Chang'e-4 rover. *Icarus*, 345: 113776.
- Gou, S., Yue, Z., Di, K., et al., 2020b. Impact melt breccia and surrounding regolith measured by Chang'e-4 rover. *Earth and Planetary Science Letters*. 544, 116378.
- Gou, S., Yue, Z., Di, K., et al., 2020c. In situ spectral measurements of space weathering by Chang'e-4 rover. *Earth and Planetary Science Letters*, 535: 116117.
- Gou, S., Yue, Z., Di, K., et al., 2021. Geologically old but freshly exposed rock fragments encountered by Yutu-2 rover. *Journal of Geophysical Research: Planets*. 126 (3), e2020JE006565.
- He, Z., Li, C., Xu, R., et al., 2019. Spectrometers based on acoustooptic tunable filters for in-situ lunar surface measurement. *J. Appl. Remote. Sens.*, 13(2): 27502.
- Hurwitz, D.M., Kring, D.A., 2014. Differentiation of the South Pole–Aitken basin impact melt sheet: Implications for lunar exploration. *Journal of Geophysical Research: Planets*. 119 (6), 1110-1133.
- Jia, M., Di, K., Yue, Z., et al., 2021. Multi-scale morphologic investigation of craters in the Chang'e-4 landing area. *Icarus*, 355: 114164.
- Jia, Y., Zou, Y., Ping, J., et al., 2018. The scientific objectives and payloads of Chang'E-4 mission. *Planetary and Space Science*, 162, 207-215.
- Li, C., Ren, X., Liu, J., et al., 2015. A New Global and High Resolution Topographic Map Product of the Moon from Chang'e-2 Image Data. *46th Lunar and Planetary Science Conference*, Abstract #1638.

- Lin, H., He, Z., Yang, W., et al., 2020a. Olivine-norite rock detected by the lunar rover Yutu-2 likely crystallized from the SPA-impact melt pool. *National Science Review*, 7:913-920.
- Lin, H., Lin, Y., Yang, W., et al., 2020b. New Insight into Lunar Regolith-forming Processes by the Lunar Rover Yutu-2. *Geophysical Research Letters*. 47 (14), e2020GL087949.
- Lin, Y., Li, X., Zhou, Y., 2021. The scientific achievements by Chang'e-4 and the new lunar samples returned by Chang'e-5. *52nd Lunar and Planetary Science Conference*, held virtually, 15-19 March, 2021. LPI Contribution No. 2548, id.2779
- Liu, B., Jia, M., Di, K., et al. 2018. Geopositioning precision analysis of multiple image triangulation using LROC NAC Lunar images. *Planetary and Space Science*, 162, 20-30.
- Liu, B., Niu, S., Xin, X., et al., 2019. High precision DTM and DOM generating using multi-source orbital data on Chang'e-4 landing site. *Int. Arch. Photogramm. Remote Sens. Spatial Inf. Sci.*, XLII-2/W13, 1413-1417.
- Liu, Z., Di, K., Peng M., et al, 2015. High precision landing site mapping and rover localization for Chang'e-3 mission. *Sci China-Phys Mech Astron*, 58(1), 019601.
- Liu, Z., Di, K., Li J., et al, 2020. Landing Site topographic mapping and rover localization for Chang'e-4 mission. *Science China-Information Sciences*, 63, 140901:1–140901:12.
- Melosh, H. J., Kendall, J., Horgan, B., et al., 2017. South Pole–Aitken basin ejecta reveal the Moon's upper mantle. *Geology*, 45(12): 1063–1066.
- Miljkovic, K., Wieczorek, M.A., Collins, G., C. Solomon, S., E. Smith, D., T. Zuber, M., 2015. Excavation of the Mantle in Basin-Forming Events on the Moon. *Earth and Planetary Science Letters*. 409, 243-251.
- Ren, X., Liu, J., Li, C., et al., 2019. A global adjustment method for photogrammetric processing of Chang'E-2 stereo images. *IEEE Transactions on Geoscience and Remote Sensing*, 57 (9), 6832-6843.
- Robinson, M., Brylow, S., Tschimmel, M., et al., 2010. Lunar Reconnaissance Orbiter Camera (LROC) instrument overview. *Space Science Reviews*, 150, 81-124.
- Smith, D. E., Zuber, M. T., Jackson, G.B., et al., 2010. The Lunar Orbiter Laser Altimeter Investigation on the Lunar Reconnaissance Orbiter Mission. *Space Science Review*, 150, 209-241.
- Speyerer, E.J., Wagner, R.V., Robinson, M.S., et al., 2016. Pre-flight and onorbit geometric calibration of the Lunar Reconnaissance Orbiter Camera. *Space Sci. Rev.*, 200, 357–392.
- Wan, W., Liu, Z., Di, K., et al., 2014. A Cross-Site Visual Localization Method for Yutu Rover. *Int. Arch. Photogramm. Remote Sens. Spatial Inf. Sci.*, XL-4, 279-284.
- Wan, W., Liu, Z., Liu, B., et al., 2019. Descent trajectory recovery of Chang'e-4 lander based on descent images. *Int. Arch. Photogramm. Remote Sens. Spatial Inf. Sci.*, XLII-2/W13, 1457-1461.
- Wang, J., Li, J., Wang, S., et al, 2020. Computer vision in the teleoperation of the Yutu-2 rover. *ISPRS Ann. Photogramm. Remote Sens. Spatial Inf. Sci.*, V-3-2020, 595–602.
- Wu, B., Liu, W. C., Grumpe, A., et al., 2018. Construction of Pixel-Level Resolution DEMs from Monocular Images by Shape and Albedo from Shading Constrained with Low-Resolution DEM. *ISPRS Journal of Photogrammetry and Remote Sensing*, 140: 3–19.
- Wu, B., Li, F., Hu, H., et al., 2020. Topographic and Geomorphological Mapping and Analysis of the Chang'E-4 Landing Site on the Far Side of the Moon. *Photogrammetric Engineering & Remote Sensing*, 86(4), 247-258.
- Wu, W., Li, C., Zuo, W., et al., 2019. Lunar farside to be explored by Chang'e-4. *Nature Geoscience*, 12(4): 222-223.
- Yang, Y., Li, S., Zhu, M.-H., Liu, Y., Wu, B., Du, J., Fa, W., Xu, R., He, Z., Wang, C., Xue, B., Yang, J., Zou, Y., 2021. Impact remnants rich in carbonaceous chondrites detected on the Moon by the Chang'e-4 rover. *Nature Astronomy*. 6, 207–213.
- Yu, T., Fei, J., Li, L., et al. 2019. Study on path planning method of lunar rover. *Journal of Deep Space Exploration*, 6(4): 384-390. (in Chinese with English abstract)
- Yu, T., Liu, Z., Rong, Z., et al., 2020. Implementation strategy of visible and near-infrared imaging spectrometer on Yutu-2 rover based on vision measurement technology. *Int. Arch. Photogramm. Remote Sens. Spatial Inf. Sci.*, XLIII-B3-2020, 1191–1197.